MATERIALS CHEMISTRY FRONTIERS

RESEARCH ARTICLE

View Article Online
View Journal | View Issue

Cite this: *Mater. Chem. Front.*, 2023, 7, 1617

Forming a composite electron blocking layer to enhance the performance of carbon-based $CsPbI_3$ perovskite solar cells†

Yongfa Song,[a] Weiping Li,*[a] Hailiang Wang,[a] Huicong Liu,[a] Yue Deng,[a] Qixian Zhang,[a] Han Rao,[a] Xiaoyu Jiang*[b] and Haining Chen*[a]

Received 1st November 2022,
Accepted 3rd February 2023

DOI: 10.1039/d2qm01124g

rsc.li/frontiers-materials

Carbon-based $CsPbI_3$ perovskite solar cells (C-PSCs) have attracted much interest due to their high chemical stability. However, their efficiency still largely lags behind those achieved by conventional $CsPbI_3$ PSCs because of the electron back transfer from the perovskite to the carbon electrode. Herein, we address the above issue by forming a composite electron blocking layer at the $CsPbI_3$/carbon interface. The $CsPbCl_3$ quantum dots (QDs) layer is first deposited on the $CsPbI_3$ film by spin coating a QDs solution, while the $Cs_2PbI_2Cl_2$ nanosheets are then generated on the surface by the post treatment of a CsCl solution. The composite blocking layer not only well suppresses electron back transfer but also passivates crystal defects. As a result, the efficiency of $CsPbI_3$ C-PSCs is boosted from 12.51% to 16.10%.

Introduction

Perovskite solar cells (PSCs) have attracted intense attention in the past few years due to their high power conversion efficiency (PCE) based on solution-based processes.[1–6] However, their low stability has greatly inhibited the commercial application of PSCs.[7–10] Generally, their low stability mainly originates from the use of organic-inorganic hybrid perovskites, made from organic hole transport materials (HTMs) and metal electrodes.[11–13] After replacing the HTM and metal electrode with a carbon electrode, carbon-based PSCs (C-PSCs) are made, and the device stability could be well improved because carbon materials are stable, inert to ion migration and inherently H_2O-resistant.[14–19]

Although C-PSCs have shown obvious enhancement in device stability, the organic components in organic-inorganic hybrid perovskites can be easily removed from the crystal structure, which still limits the device stability. In order to address the issue, researchers have introduced inorganic perovskites to replace the organic-inorganic hybrid perovskites as light absorbers in C-PSCs.[20–25] Among various inorganic perovskites, $CsPbI_3$ has shown great prospects duo to the suitable bandgap of 1.73 eV.[26–32] So far, great progress has been made on $CsPbI_3$ C-PSCs and over 16% PCE has been achieved.[33]

However, the above PCE still largely lags behind those achieved by the conventional $CsPbI_3$ PSCs (about 21%).[34] The low hole selectivity of the carbon electrode is the main cause because the photogenerated electrons tend to transfer to the carbon electrode for inducing serious recombination loss.[11,35] To suppress the electron back transport, forming an electron blocking layer at the $CsPbI_3$/carbon interface has been employed.[36–38] For example, phenylethylamine iodide (PEAI)[39] or CsCl[40] have been used to treat the $CsPbI_3$ layer to grow a 2D perovskite layer *in situ* acting as an electron blocking layer. However, the performance improvement is still limited for a single electron blocking layer and a new strategy is needed.

Herein, both $CsPbCl_3$ QDs and 2D $Cs_2PbI_2Cl_2$ were deposited on the $CsPbI_3$ perovskite layer to form a composite electron blocking layer. Firstly, $CsPbCl_3$ QDs were spin coated on the $CsPbI_3$ perovskite layer by using a $CsPbCl_3$ QDs cyclohexane solution. Then, a CsCl ethanol solution was also spin coated on the QDs-coated $CsPbI_3$ perovskite layer to form 2D $Cs_2PbI_2Cl_2$. Such architecture forms a favorable energy level alignment for electron blocking. In addition, crystal defects were also effectively passivated. As a result, the PCE of $CsPbI_3$ C-PSCs was promoted from 12.51% to 16.10%.

Results and discussion

The $CsPbCl_3$ QDs were synthesized using the thermal injection method described in the Experimental section.[41,42] The TEM image in Fig. S1a (ESI†) shows that the $CsPbCl_3$ QDs have a regular square structure with a size of about 12 nm. The X-ray

[a] No. 37 Xueyuan Road, Haidian District, Beijing 100191, People's Republic of China. E-mail: liweiping@buaa.edu.cn, chenhaining@buaa.edu.cn
[b] Beijing 100072, People's Republic of China. E-mail: jiangxiaoyu2007@gmail.com

† Electronic supplementary information (ESI) available. See DOI: https://doi.org/10.1039/d2qm01124g

diffraction (XRD) pattern in Fig. S1b (ESI†) indicates that all diffraction peaks match well with the tetragonal structure of the $CsPbCl_3$ perovskite (JCPDS 18-0366).[19] Therefore, $CsPbCl_3$ QDs have been successfully prepared.

For preparing the $CsPbI_3$ perovskite films, a precursor solution containing CsI, PbI_2 and DMAI was spin coated on the TiO_2 substrate, followed by annealing at 220 °C for 5 min. After the deposition of the $CsPbI_3$ perovskite films, three kinds of samples were obtained by the processes illustrated in Fig. 1. For the $CsPbI_3$–CsCl film, the as-deposited $CsPbI_3$ perovskite films were treated with a CsCl ethanol solution (1 mg ml^{-1}) by spin coating. For the $CsPbI_3$-QDs film, a $CsPbCl_3$ QDs cyclohexane solution was spin-coated on the as-deposited $CsPbI_3$ perovskite film. For the $CsPbI_3$-QDs/CsCl film, the as-deposited $CsPbI_3$ perovskite films were successively treated with a $CsPbCl_3$ QDs solution and CsCl solution.

Scanning electron microscopy (SEM) was employed to evaluate the film morphology (Fig. 2 and Fig. S2, ESI†). The control $CsPbI_3$ film exhibits uniform morphology (Fig. 2a). 2D nanosheets estimated to be around 200–350 nm in width appear on the surface of the $CsPbI_3$–CsCl film (Fig. 2b and f). They are uniformly distributed on the surface and are perpendicular to the surface of the perovskite film. The $CsPbCl_3$ QDs are uniformly distributed on the surface of the QDs film after spin-coating the $CsPbCl_3$ QDs solution (Fig. 2c and g). After depositing the $CsPbCl_3$ QDs, the $CsPbI_3$-QDs film show a denser and more uniform surface morphology. For the $CsPbI_3$-QDs/CsCl film, the $CsPbCl_3$ QDs are uniformly dispersed and 2D nanosheets are also generated on the surface, forming a 2D/0D electron blocking layer. Atomic force microscopy (AFM) was further used to reveal the morphology change. The roughness of the QDs film is reduced from 41.8 to 28.6 nm compared with control $CsPbI_3$ film, while the roughness of the $CsPbI_3$-QDs/CsCl film is reduced from 72.5 to 48.1 nm compared with the control CsCl film, indicating that the $CsPbCl_3$ QDs are more easily deposited at the grain boundary and reduce the surface roughness, which is conducive to the contact between $CsPbI_3$ and the carbon electrode.

The X-ray diffraction (XRD) patterns in Fig. 3a reveal that the control $CsPbI_3$ film exhibits two intense peaks at 14.3° and 28.8°, which are assignable to the (110) and (220) peaks of the $CsPbI_3$ perovskite, respectively. After post treatment with CsCl solution, an additional peak is observed at 9.5°. As reported in our previous work, this peak corresponds to the (002) plane of 2D $Cs_2PbI_2Cl_2$, resulting from the reaction between CsCl and $CsPbI_3$.[40,43] For the $CsPbI_3$-QDs film, the peak corresponding to $CsPbCl_3$ appear. As expected, both $Cs_2PbI_2Cl_2$ and $CsPbCl_3$ peaks are found for the $CsPbI_3$-QDs/CsCl films. For more detailed observations in Fig. S3 (ESI†), the characteristic peaks of $CsPbI_3$ perovskite shift to a larger angle after QDs or CsCl treatment, implying the partial replacement of I^- ions with Cl^- ions.[44,45]

X-ray photoelectron spectroscopy (XPS) measurements were further carried out to evaluate the composition of different $CsPbI_3$ films. As shown in Fig. S4 (ESI†), compared with the control $CsPbI_3$ film, the characteristic peaks of Cl 2p appeared in the $CsPbI_3$–CsCl, -QDs and -QDs/CsCl films,[45,46] indicating that Cl has been incorporated after post treatment. Due to the difference in the chemical environment of the Cl element, compared with the $CsPbI_3$–CsCl film, the Cl 2p peak shifts to a lower binding energy for the $CsPbI_3$-QDs film. As expected, the Cl 2p in the $CsPbI_3$-QDs/CsCl films can be deconvolved into two sets of Cl 2p peaks, corresponding to the presence of $CsPbCl_3$ QDs and $Cs_2PbI_2Cl_2$ nanosheets. Similarly, the Pb 4f peaks can also be deconvolved into two sets of Pb 4f peaks. (Fig. 2d).

Ultraviolet-visible (UV-Vis) absorption spectra were subsequently measured for different films. As shown in Fig. 4a, the pristine $CsPbI_3$ film shows the absorption onset at around 741 nm. Due to the partial replacement of I with Cl, the absorption onset of the $CsPbI_3$–CsCl film blue shifts to about 737 nm. Similarly, a blue shift is also observed for the absorption onset of the $CsPbI_3$-QDs film (about 735 nm). More

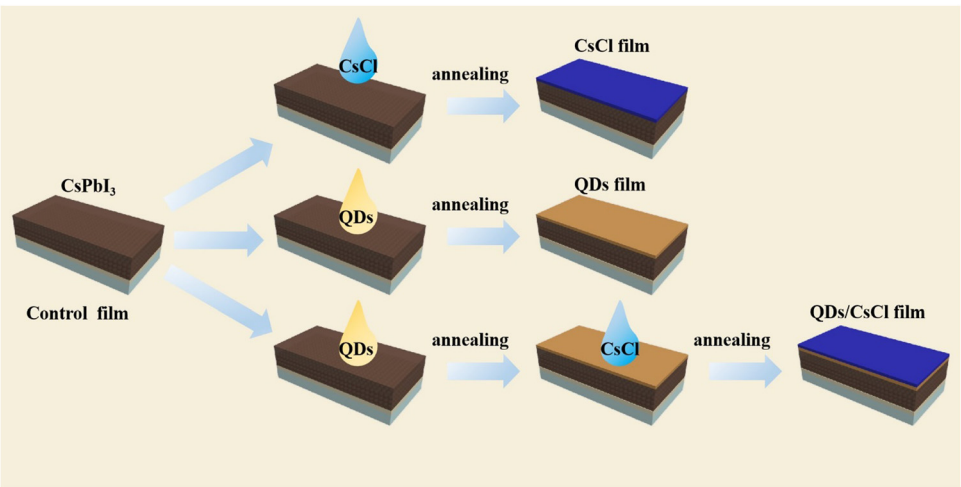

Fig. 1 Schematic illustrating the deposition processes of the $CsPbI_3$–CsCl, $CsPbI_3$-QDs and $CsPbI_3$-QDs/CsCl films.

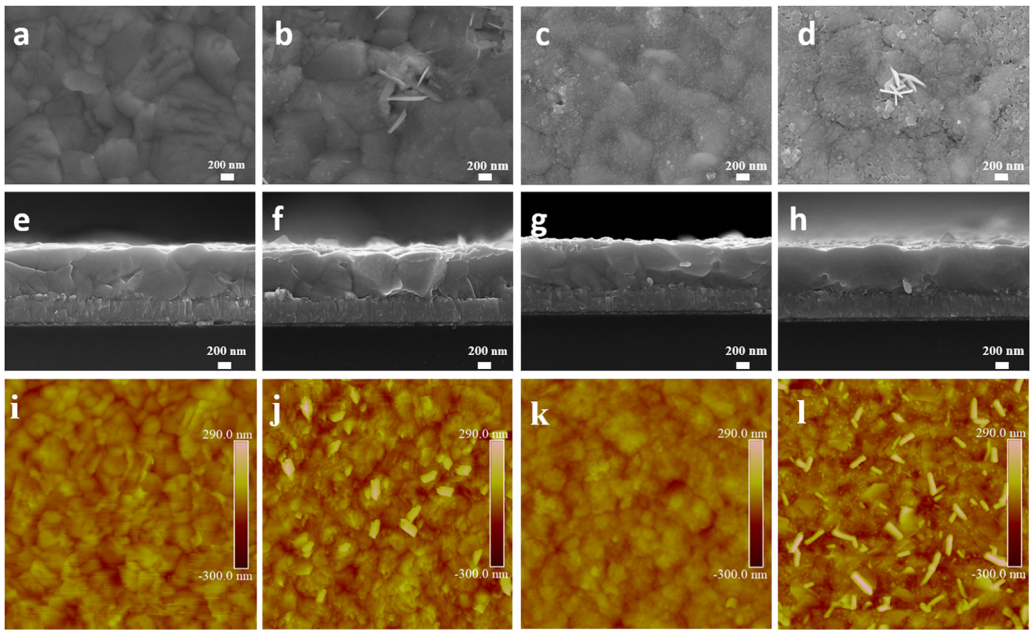

Fig. 2 SEM images of the (e and a) control, (b and f) $CsPbI_3$–CsCl, (c and g) $CsPbI_3$-QDs, and (d and h) $CsPbI_3$-QDs/CsCl films; AFM images of different perovskite films: (i) $CsPbI_3$, (j) $CsPbI_3$–CsCl, (k) $CsPbI_3$-QDs, and (l) $CsPbI_3$-QDs/CsCl films.

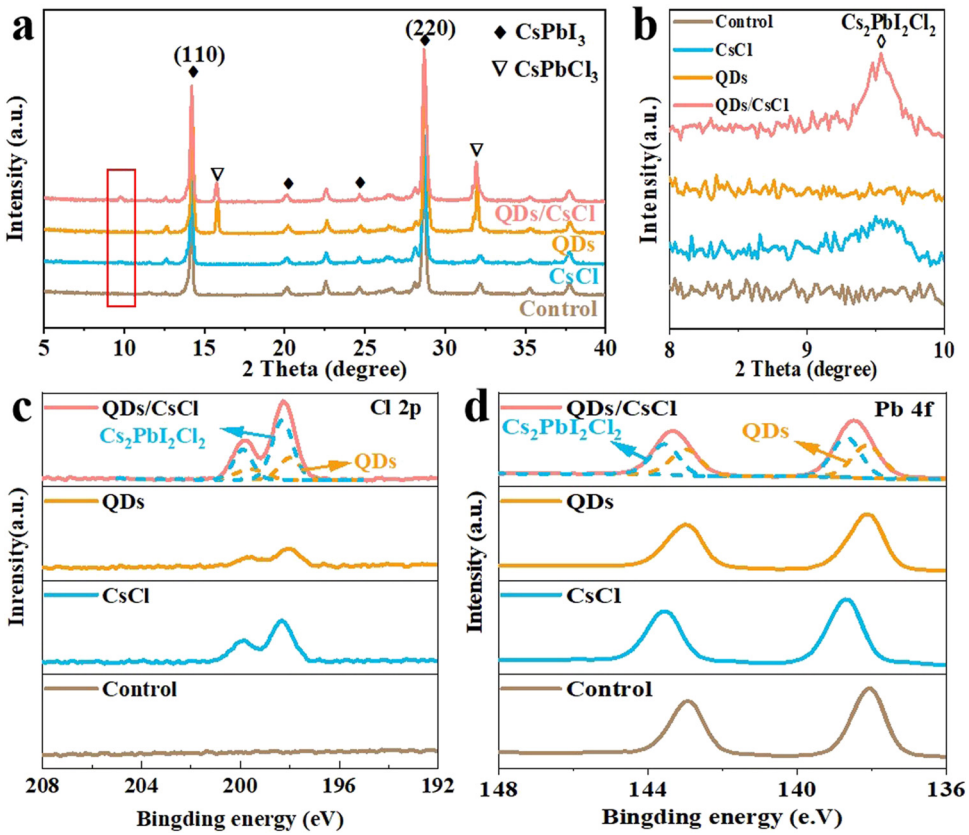

Fig. 3 (a) XRD patterns and (b) magnified XRD patterns (in the 2θ ranges of 8–10°) of different $CsPbI_3$ films. XPS spectra of (c) Cl 2p and (d) Pb 4f for different $CsPbI_3$ films.

obviously, the absorption onset of the $CsPbI_3$-QDs/CsCl film blue shifts to about 734 nm. According to Tauc plots in Fig. S5 (ESI†), *Eg* for the pristine $CsPbI_3$, $CsPbI_3$–CsCl, $CsPbI_3$-QDs and $CsPbI_3$-QDs/CsCl films are calculated to be 1.671, 1.683, 1.686

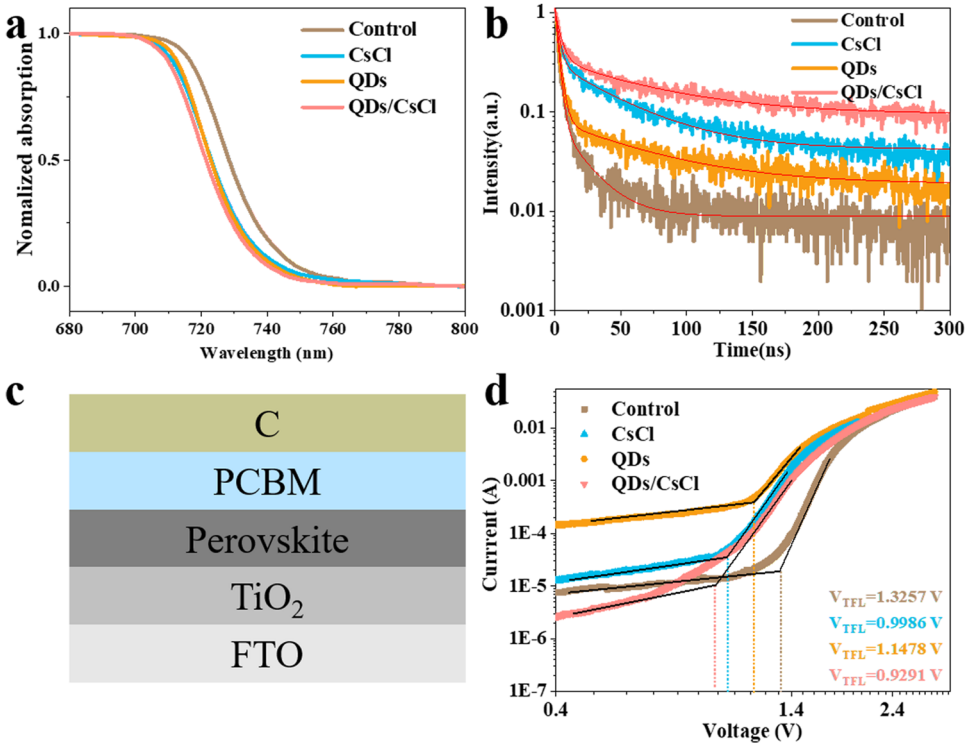

Fig. 4 (a) UV-Vis, (b) TRPL spectra, (c) architecture of the electro-only device for SCLC, and (d) SCLC results for different $CsPbI_3$ films.

and 1.688 eV, respectively. The confocal PL mappings in Fig. S6 (ESI†) further confirm the above phenomenon.

Time-resolved photoluminescence decay (TRPL) spectra were also taken for different films (Fig. 4b). By fitting the TRPL spectra with a double exponential decay model, the average lifetime (τ_{ave}) of the different films could be calculated. As shown in Table S1 (ESI†), the τ_{ave} of the control $CsPbI_3$ film is 8.87 ns, while the τ_{ave} of the $CsPbI_3$–CsCl, -QDs and -QDs/CsCl films are obviously increased to 40.60 ns, 38.94 ns and 60.24 ns, respectively. Therefore, post treatment has well prolonged the carrier lifetime due to the reduced defect density, especially for the $CsPbI_3$-QDs/CsCl film.[47]

Space charge limited current (SCLC) measurements were performed by constructing an electron-only device of FTO/TiO_2/$CsPbI_3$/PCBM/C (Fig. 4c). According to the dark J–V curve (Fig. 4d), the trap density (n_t) can be calculated by the trap-filled limit voltage (V_{TFL}).

$$n_t = 2\varepsilon_0\varepsilon V_{TFL}/ed^2 \quad (1)$$

where ε_0 is the vacuum dielectric constant, ε is the relative dielectric constant of perovskite, d is the film thickness, e is the basic charge, and n_t is the density of trapped states.[48] The trap density values were calculated to be 1.807×10^{15}, 1.361×10^{15}, 1.564×10^{15} and 1.266×10^{15} cm^{-3} for the pristine $CsPbI_3$, $CsPbI_3$–CsCl, $CsPbI_3$-QDs and $CsPbI_3$-QDs/CsCl films, respectively. Therefore, the SCLC results further confirm that the post treatment processes have well reduced the trap density, especially for the $CsPbI_3$-QDs/CsCl film.

$CsPbI_3$ C-PSCs were fabricated by directly painting commercial carbon paste on the perovskite films, followed by annealing 120 °C (Fig. 5a). All processes were carried out in dry air. Fig. 5b show the architecture of the $CsPbI_3$ C-PSCs: FTO/c-TiO_2/m-TiO_2/$CsPbI_3$/carbon and the cross-sectional SEM image in Fig. 5c indicates the close contact at the $CsPbI_3$/carbon interface. The current density-voltage (J–V) curves in Fig. 5d and Table S2 (ESI†) indicate that the control device achieves a PCE of 12.51% with a V_{oc} of 1.081 V, J_{sc} of 16.46 mA cm^{-2} and FF of 0.703. After treatment with CsCl, the $CsPbI_3$–CsCl PSCs device displays a PCE of 13.65% with a V_{oc} of 1.099, J_{sc} of 17.67 mA cm^{-2} and FF of 0.703. The $CsPbI_3$-QDs device displays a PCE of 14.18% with a V_{oc} of 1.105, J_{sc} of 18.14 mA cm^{-2} and FF of 0.708. Interestingly, the PCE of the $CsPbI_3$-QDs/CsCl device is significantly improved to 16.10% with a V_{oc} of 1.137 V, J_{sc} of 18.74 mA cm^{-2} and FF of 0.755, respectively. As noted, the large improvement in the PCE for the $CsPbI_3$-QDs/CsCl device is mainly attributed to the increase in V_{oc} and FF, which should originate from the improvement in energy level alignment and the reduction in the surface roughness. The J–V curves obtained from forward and reverse scans (Fig. S7, ESI†) and the steady-state power output for the $CsPbI_3$-QDs/CsCl device demonstrate the small hysteresis and stable power output (Fig. S7, ESI†). The device stability was tested at 85 °C in N_2 conditions (Fig. S8, ESI†). The QDs/CsCl device maintains over 95% of its initial PCE after 140 h, while the PCE of the pristine device declines to about 84%.

Mott–Schottky (M–S) plots (Fig. 5e) were taken for different devices to obtain the built-in potential (V_{bi}). The V_{bi} for the

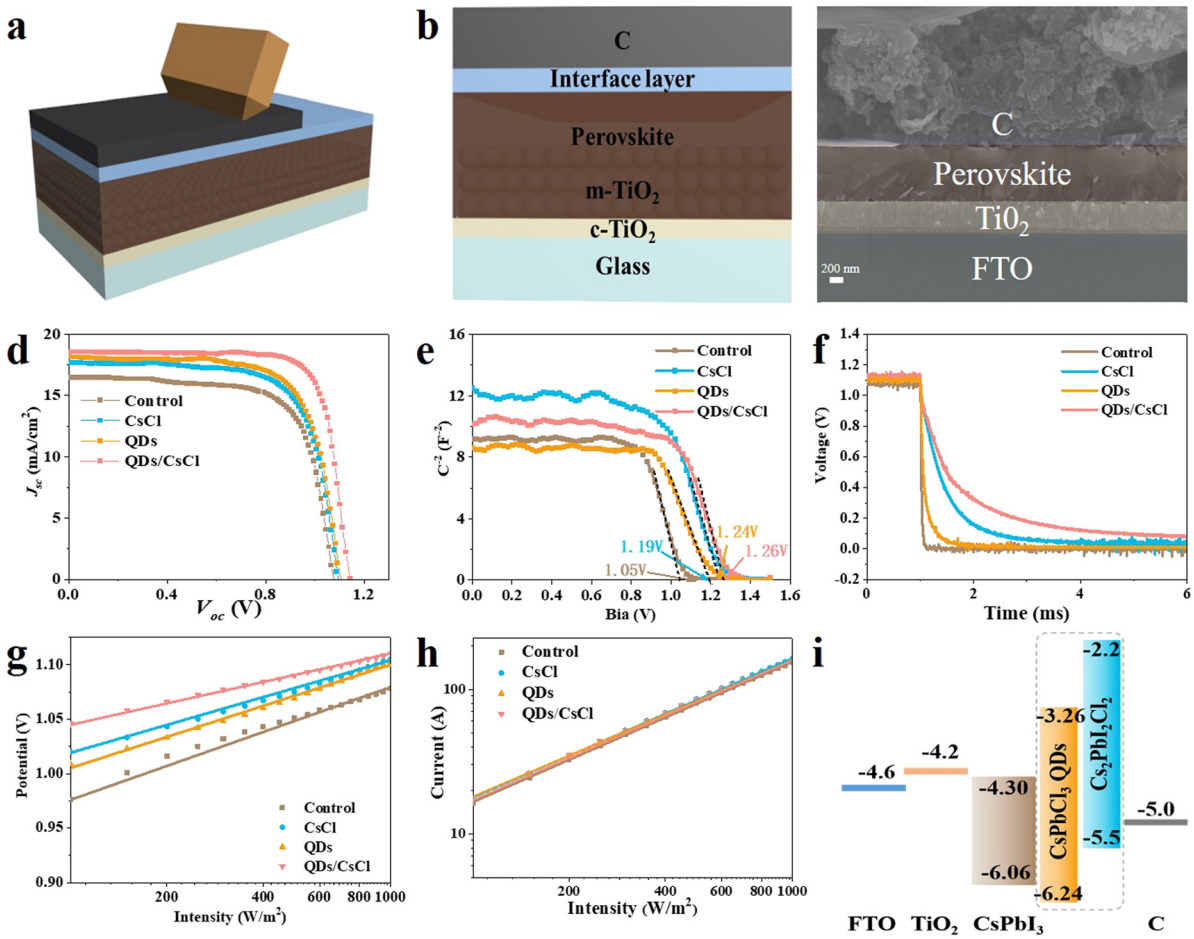

Fig. 5 Schematic diagram of (a) the fabrication process of carbon electrode and (b) device structure; (c) cross-section SEM image of $CsPbI_3$ C-PSCs; (d) *J*–*V* curves, (e) Mott–Schottky plots obtained at 10 kHz, (f) TPV, (g) dependence of V_{oc} on *I*, and (h) dependence of J_{sc} on *I* for different devices; (i) Energy level diagrams of the $CsPbI_3$-QDs/CsCl C-PSCs.

pristine $CsPbI_3$ device is calculated to be about 1.06 V. After post treatment, all devices show increased V_{bi} and the highest V_{bi} of 1.26 V is achieved for the $CsPbI_3$-QDs/CsCl device. The higher V_{bi} provides a larger driving force for carrier separation and collection, which is favorable for achieving higher V_{oc} and FF. The transient photo-voltage decay (TPV) results in Fig. 5f indicate that the $CsPbI_3$-QDs/CsCl device shows the slowest decay, further proving the most effective charge separation and the least charge recombination. The dark *J*–*V* curves of the pristine and QDs/CsCl devices are shown in Fig. S9 (ESI†). The QDs/CsCl device exhibits a much lower dark current density compared with the pristine device under a positive bias voltage, indicating that in the QDs/CsCl device the composite electron blocking layer well suppressed the back transfer of electrons from the perovskite to the carbon electrode.

The light intensity dependence of J_{sc} and V_{oc} are shown in Fig. 5g and h, respectively. The recombination mechanism can be understood according to eqn (2) and (3).

$$J_{sc} \propto I^{\alpha} \ (\alpha \leq 1) \quad (2)$$

$$V_{oc} = \varepsilon(K_B T/e)\ln(I) + \text{constant} \quad (3)$$

where *I* is the light intensity, α is the exponential factor, ε is the ideality factor, K_B is the Boltzmann constant, *T* is the absolute temperature and the *e* is elementary charge. The α values are fitted and calculated to be 0.97, 0.96, 0.96 and 0.96 for the $CsPbI_3$, $CsPbI_3$–CsCl, $CsPbI_3$-QDs and $CsPbI_3$-QDs/CsCl devices, respectively. The α values closer to 1, indicate more effective charge separation and lower nonradiative recombination. The ε for the control $CsPbI_3$, $CsPbI_3$–CsCl, -QDs and -QDs/CsCl devices are calculated to be 1.79, 1.40, 1.53 and 1.28, respectively, which demonstrates that trap-assisted recombination has been well suppressed in the $CsPbI_3$-QDs/CsCl device.

Conclusion

We have formed a composite electron blocking layer ($CsPbCl_3$ QDs/$Cs_2PbI_2Cl_2$) on the $CsPbI_3$ film structure by successively treating the film with $CsPbCl_3$ QDs and CsCl solutions. Such architecture forms a favorable energy level alignment for electron blocking. Furthermore, the crystal defects of the $CsPbI_3$ film were also effectively passivated. As a result, the PCE of $CsPbI_3$ C-PSCs was promoted from 12.51% to 16.10%.

Conflicts of interest

There are no conflicts to declare.

Acknowledgements

This work was supported by the National Natural Science Foundation of China (51971012).

References

1 C. Liu, J. He, M. Wu, Y. Wu, P. Du, L. Fan, Q. Zhang, D. Wang and T. Zhang, All-Inorganic CsPbI2Br Perovskite Solar Cell with Open-Circuit Voltage over 1.3 V by Balancing Electron and Hole Transport, *Sol. RRL*, 2020, **4**, 2000016.
2 Q. Tai, K.-C. Tang and F. Yan, Recent progress of inorganic perovskite solar cells, *Energy Environ. Sci.*, 2019, **12**, 2375–2405.
3 M. Chen, M.-G. Ju, H. F. Garces, A. D. Carl, L. K. Ono, Z. Hawash, Y. Zhang, T. Shen, Y. Qi, R. L. Grimm, D. Pacifici, X. C. Zeng, Y. Zhou and N. P. Padture, Highly stable and efficient all-inorganic lead-free perovskite solar cells with native-oxide passivation, *Nat. Commun.*, 2019, **10**, 16.
4 A. Ho-Baillie, M. Zhang, C. F. J. Lau, F.-J. Ma and S. Huang, Untapped Potentials of Inorganic Metal Halide Perovskite Solar Cells, *Joule*, 2019, **3**, 938–955.
5 Z. Chen, Q. Dong, Y. Liu, C. Bao, Y. Fang, Y. Lin, S. Tang, Q. Wang, X. Xiao, Y. Bai, Y. Deng and J. Huang, Thin single crystal perovskite solar cells to harvest below-bandgap light absorption, *Nat. Commun.*, 2017, **8**, 1890.
6 L. Qiu, S. He, L. K. Ono, S. Liu and Y. Qi, Scalable Fabrication of Metal Halide Perovskite Solar Cells and Modules, *ACS Energy Lett.*, 2019, **4**, 2147–2167.
7 G. Tong, L. K. Ono and Y. Qi, Recent Progress of All-Bromide Inorganic Perovskite Solar Cells, *Energy Technol.*, 2020, **8**, 1900961.
8 J. Y. Kim, J.-W. Lee, H. S. Jung, H. Shin and N.-G. Park, High-Efficiency Perovskite Solar Cells, *Chem. Rev.*, 2020, **120**, 7867–7918.
9 H. Wang, Z. Dong, H. Liu, W. Li, L. Zhu and H. Chen, Roles of Organic Molecules in Inorganic CsPbX3 Perovskite Solar Cells, *Adv. Energy Mater.*, 2021, **11**, 2002940.
10 Y. Li, H. Xie, E. L. Lim, A. Hagfeldt and D. Bi, Recent Progress of Critical Interface Engineering for Highly Efficient and Stable Perovskite Solar Cells, *Adv. Energy Mater.*, 2022, **12**, 2102730.
11 H. Chen and S. Yang, Methods and strategies for achieving high-performance carbon-based perovskite solar cells without hole transport materials, *J. Mater. Chem. A*, 2019, **7**, 15476–15490.
12 D. Bogachuk, S. Zouhair, K. Wojciechowski, B. Yang, V. Babu, L. Wagner, B. Xu, J. Lim, S. Mastroianni, H. Pettersson, A. Hagfeldt and A. Hinsch, Low-temperature carbon-based electrodes in perovskite solar cells, *Energy Environ. Sci.*, 2020, **13**, 3880–3916.
13 H. Chen and S. Yang, Carbon-Based Perovskite Solar Cells without Hole Transport Materials: The Front Runner to the Market?, *Adv. Mater.*, 2017, **29**, 1603994.
14 X. Zhang, Z. Yu, D. Zhang, Q. Tai and X.-Z. Zhao, Recent Progress of Carbon-Based Inorganic Perovskite Solar Cells: From Efficiency to Stability, *Adv. Energy Mater.*, 2022, 2201320.
15 B. Conings, J. Drijkoningen, N. Gauquelin, A. Babayigit, J. D'Haen, L. D'Olieslaeger, A. Ethirajan, J. Verbeeck, J. Manca, E. Mosconi, F. D. Angelis and H.-G. Boyen, Intrinsic Thermal Instability of Methylammonium Lead Trihalide Perovskite, *Adv. Energy Mater.*, 2015, **5**, 1500477.
16 J. K. Nam, S. U. Chai, W. Cha, Y. J. Choi, W. Kim, M. S. Jung, J. Kwon, D. Kim and J. H. Park, Potassium Incorporation for Enhanced Performance and Stability of Fully Inorganic Cesium Lead Halide Perovskite Solar Cells, *Nano Lett.*, 2017, **17**, 2028–2033.
17 P. Yu, W. Zhang, F. Ren, J. Wang, H. Wang, R. Chen, S. Zhang, Y. Zhang, Z. Liu and W. Chen, Strategies for highly efficient and stable cesium lead iodide perovskite photovoltaics: mechanisms and processes, *J. Mater. Chem. C*, 2022, **10**, 4999–5023.
18 Y. Zhao, J. Duan, Y. Wang, X. Yang and Q. Tang, Precise stress control of inorganic perovskite films for carbon-based solar cells with an ultrahigh voltage of 1.622 V, *Nano Energy*, 2020, **67**, 104286.
19 X. Chang, W. Li, L. Zhu, H. Liu, H. Geng, S. Xiang, J. Liu and H. Chen, Carbon-Based CsPbBr3 Perovskite Solar Cells: All-Ambient Processes and High Thermal Stability, *ACS Appl. Mater. Interfaces*, 2016, **8**, 33649–33655.
20 Z. Yao, W. Zhao and S. Liu, Stability of the CsPbI3 perovskite: from fundamentals to improvements, *J. Mater. Chem. A*, 2021, **9**, 11124–11144.
21 Z. Dong, W. Li, H. Wang, X. Jiang, H. Liu, L. Zhu and H. Chen, High-Temperature Perovskite Solar Cells, *Sol. RRL*, 2021, **5**, 2100370.
22 W. Zhu, J. Ma, W. Chai, T. Han, D. Chen, X. Xie, G. Liu, P. Dong, H. Xi, D. Chen, J. Zhang, C. Zhang and Y. Hao, Intermediate Phase-Assisted Sequential Deposition Toward 15.24%-Efficiency Carbon-Electrode Cspbi2br Perovskite Solar Cells, *Sol. RRL*, 2022, **6**, 2200020.
23 H. Wang, S. Xiang, W. Li, H. Liu, L. Zhu, S. Xiao, S. Yang and H. Chen, Skillfully deflecting the question: a small amount of piperazine-1,4-diium iodide radically enhances the thermal stability of CsPbI3 perovskite, *J. Mater. Chem. C*, 2019, **7**, 11757–11763.
24 C. Dong, B. Xu, D. Liu, E. G. Moloney, F. Tan, G. Yue, R. Liu, D. Zhang, W. Zhang and M. I. Saidaminov, Carbon-based all-inorganic perovskite solar cells: Progress, challenges and strategies toward 20% efficiency, *Mater. Today*, 2021, **50**, 239–258.
25 S. Xiang, W. Li, Y. Wei, J. Liu, H. Liu, L. Zhu and H. Chen, The synergistic effect of non-stoichiometry and Sb-doping on air-stable α-CsPbI3 for efficient carbon-based perovskite solar cells, *Nanoscale*, 2018, **10**, 9996–10004.
26 R. J. Sutton, G. E. Eperon, L. Miranda, E. S. Parrott, B. A. Kamino, J. B. Patel, M. T. Hörantner, M. B. Johnston,

A. A. Haghighirad, D. T. Moore and H. J. Snaith, Bandgap-Tunable Cesium Lead Halide Perovskites with High Thermal Stability for Efficient Solar Cells, *Adv. Energy Mater.*, 2016, **6**, 1502458.

27 A. Miyata, A. Mitioglu, P. Plochocka, O. Portugall, J. T.-W. Wang, S. D. Stranks, H. J. Snaith and R. J. Nicholas, Direct measurement of the exciton binding energy and effective masses for charge carriers in organic–inorganic tri-halide perovskites, *Nat. Phys.*, 2015, **11**, 582–587.

28 Z. Shao, H. Meng, X. Du, X. Sun, P. Lv, C. Gao, Y. Rao, C. Chen, Z. Li, X. Wang, G. Cui and S. Pang, Cs4PbI6-Mediated Synthesis of Thermodynamically Stable FA0.15Cs0.85PbI3 Perovskite Solar Cells, *Adv. Mater.*, 2020, **32**, 2001054.

29 J. Liu, L. Zhu, S. Xiang, H. Wang, H. Liu, W. Li and H. Chen, Cs-Doped TiO2 Nanorod Array Enhances Electron Injection and Transport in Carbon-Based CsPbI3 Perovskite Solar Cells, *ACS Sustainable Chem. Eng.*, 2019, **7**, 16927–16932.

30 X. Fu, K. Zhou, X. zhou, H. Ji, Y. Min and Y. Qian, Surface passivation for enhancing photovoltaic performance of carbon-based CsPbI3 perovskite solar cells, *J. Solid State Chem.*, 2022, **308**, 122891.

31 R. Yin, K.-X. Wang, X.-N. Huo, Y.-S. Sun, W.-W. Sun, Y.-K. Gao, T.-T. You and P.-G. Yin, A One-Step Ionic Liquid Interface-to-Bulk Modification for Stable Carbon-Based CsPbI3 Perovskite Solar Cells with Efficiency Over 15%, *Adv. Mater. Interfaces*, 2022, **9**, 2201488.

32 S. Xiang, W. Li, Y. Wei, J. Liu, H. Liu, L. Zhu, S. Yang and H. Chen, Natrium Doping Pushes the Efficiency of Carbon-Based CsPbI3 Perovskite Solar Cells to 10.7%, *iScience*, 2019, **15**, 156–164.

33 H. Wang, H. Liu, Z. Dong, X. Wei, W. Li, L. Zhu, C. Zhu, Y. Bai and H. Chen, Moisture is not always bad: H2O accelerates the conversion of DMAPbI3 intermediate to CsPbI3 for boosting the efficiency of carbon-based perovskite solar cells to over 16%, *Fundam. Res.*, 2022, DOI: 10.1016/j.fmre.2022.07.005.

34 Y. Cui, J. Shi, F. Meng, B. Yu, S. Tan, S. He, C. Tan, Y. Li, H. Wu, Y. Luo, D. Li and Q. Meng, A Versatile Molten-Salt Induction Strategy to Achieve Efficient CsPbI3 Perovskite Solar Cells with a High Open-Circuit Voltage >1.2 V, *Adv. Mater.*, 2022, 2205028.

35 Z. Dong, W. Li, H. Wang, X. Jiang, H. Liu, L. Zhu and H. Chen, Carbon nanotubes in perovskite-based optoelectronic devices, *Matter*, 2022, **5**, 448–481.

36 S. Zouhair, S.-M. Yoo, D. Bogachuk, J. P. Herterich, J. Lim, H. Kanda, B. Son, H. J. Yun, U. Würfel, A. Chahboun, M. K. Nazeeruddin, A. Hinsch, L. Wagner and H. Kim, Employing 2D-Perovskite as an Electron Blocking Layer in Highly Efficient (18.5%) Perovskite Solar Cells with Printable Low Temperature Carbon Electrode, *Adv. Energy Mater.*, 2022, **12**, 2200837.

37 X.-N. Huo, K.-X. Wang, R. Yin, W.-W. Sun, Y.-S. Sun, Y.-K. Gao, T.-T. You and P.-G. Yin, High-performance carbon-based all-inorganic CsPbI2Br perovskite solar cells via ethylammonium iodide and phenethylammonium iodide synergistic passivation, *Sol. Energy Mater. Sol. Cells*, 2022, **247**, 111963.

38 J. Zhou, Z. Ye, J. Hou, J. Wu, Y.-Z. Zheng and X. Tao, Efficient ambient-air-stable HTM-free carbon-based perovskite solar cells with hybrid 2D–3D lead halide photoabsorbers, *J. Mater. Chem. A*, 2018, **6**, 22626–22635.

39 K. Wang, Z. Li, F. Zhou, H. Wang, H. Bian, H. Zhang, Q. Wang, Z. Jin, L. Ding and S. Liu, Ruddlesden–Popper 2D Component to Stabilize γ-CsPbI3 Perovskite Phase for Stable and Efficient Photovoltaics, *Adv. Electron. Mater.*, 2019, **9**, 1902529.

40 H. Wang, H. Liu, Z. Dong, W. Li, L. Zhu and H. Chen, Composition manipulation boosts the efficiency of carbon-based CsPbI3 perovskite solar cells to beyond 14%, *Nano Energy*, 2021, **84**, 105881.

41 A. De, N. Mondal and A. Samanta, Luminescence tuning and exciton dynamics of Mn-doped CsPbCl3 nanocrystals, *Nanoscale*, 2017, **9**, 16722–16727.

42 Y. Su, X. Chen, W. Ji, Q. Zeng, Z. Ren, Z. Su and L. Liu, Highly Controllable and Efficient Synthesis of Mixed-Halide CsPbX3 (X = Cl, Br, I) Perovskite QDs toward the Tunability of Entire Visible Light, *ACS Appl. Mater. Interfaces*, 2017, **9**, 33020–33028.

43 X. Zhao, T. Liu, Q. C. Burlingame, T. Liu, R. Holley, G. Cheng, N. Yao, F. Gao and Y.-L. Loo, Accelerated aging of all-inorganic, interface-stabilized perovskite solar cells, *Science*, 2022, **377**, 307–310.

44 S. Yang, W. Liu, Y. Han, Z. Liu, W. Zhao, C. Duan, Y. Che, H. Gu, Y. Li and S. Liu, 2D Cs2PbI2Cl2 Nanosheets for Holistic Passivation of Inorganic CsPbI2Br Perovskite Solar Cells for Improved Efficiency and Stability, *Adv. Energy Mater.*, 2020, **10**, 2002882.

45 T. V. Vu, A. A. Lavrentyev, B. V. Gabrelian, K. D. Pham, O. V. Parasyuk, N. M. Denysyuk and O. Y. Khyzhun, Electronic structure and optical constants of CsPbCl3: The effect of approaches within ab initio calculations in relation to X-ray spectroscopy experiments, *Mater. Chem. Phys.*, 2021, **261**, 124216.

46 Z. Zhao, W. Xu, G. Pan, Y. Liu, M. Yang, S. Hua, X. Chen, H. Peng and H. Song, Enhancing the exciton emission of CsPbCl3 perovskite quantum dots by incorporation of Rb^+ ions, *Mater. Res. Bull.*, 2019, **112**, 142–146.

47 Y. Zhang, Z. Li, H. Chen, Y. Xu, Y. Lei, G. Peng, X. Zhou, Q. Wang and Z. Jin, Double-Layer Quantum Dots as Interfacial Layer to Enhance the Performance of CsPbI3 Solar Cells, *Adv. Mater. Interfaces*, 2022, 2200813.

48 V. M. Le Corre, E. A. Duijnstee, O. El Tambouli, J. M. Ball, H. J. Snaith, J. Lim and L. J. A. Koster, Revealing Charge Carrier Mobility and Defect Densities in Metal Halide Perovskites via Space-Charge-Limited Current Measurements, *ACS Energy Lett.*, 2021, **6**, 1087–1094.